Transition Strategies for Tilt-Wing Aircraft

Marc May* and Daniel Milz[†]
Institute of System Dynamics and Control, German Aerospace Center (DLR), 82234 Weßling, Germany
TUM School of Engineering and Design, eAviation Professorship, 85521 Ottobrunn, Germany

Sophie Armanini [‡]
TUM School of Engineering and Design, eAviation Professorship, 85521 Ottobrunn, Germany

Gertjan Looye[§]
Institute of System Dynamics and Control, German Aerospace Center (DLR), 82234 Weßling, Germany

Tilt-wing aircraft promise to combine cruise efficiency with vertical take-off and landing capability. However, this introduces the complex but crucial transition flight phase, which is not yet well understood regarding aerodynamics and flight dynamics. To better understand the aircraft dynamic behavior within this flight regime, this paper analyzes the longitudinal tilt-wing transition, considering various operational strategies for the maneuver. The analysis is based on an optimal control approach where the dynamic control problem is transcribed into a nonlinear programming (NLP) problem. The developed framework allows for successfully exploring different transition strategies by adapting constraints and objective functions. Compared to the results of static trim analyses, the phenomena of transition folds are attenuated in the dynamic investigation due to inertial effects. Furthermore, the backward transition maneuver from cruise to hover flight proves to be more challenging from a flight physics perspective because of high effective angles of attack, and requires upward motion if flow separation is to be avoided.

Nomenclature

b, c = wing span and chord, m

C_L, C_D, C_M = aerodynamic coefficient for lift, drag, pitch moment

$\boldsymbol{c}$ = constraint vector

$\boldsymbol{c}_d$ = defect constraints

$\boldsymbol{c}_l, \boldsymbol{c}_u$ = upper and lower constraint limits

---

Presented as Paper 2024-1289 at the AIAA SciTech 2024 Forum, Orlando,FL, January 8–12, 2024;

*Research Assistant, Institute of System Dynamics and Control; marc.may@dlr.de, AIAA member
[†]Research Assistant, Institute of System Dynamics and Control; daniel.milz@dlr.de, AIAA member
[‡]Professor, TUM School of Engineering and Design, eAviation Professorship
[§]Head of Department, Institute of System Dynamics and Control; gertjan.looye@dlr.de, AIAA member

d_s = distance between propeller plane and wing quarter line, m

$F^B_{A,x}, F^B_{A,z}$ = aerodynamic force in body x and z direction, N

$\boldsymbol{f}_A$ = aerodynamic force vector, N

$\boldsymbol{G}$ = Jacobian

g = gravitational acceleration, $\mathrm{m\,s^{-2}}$

$\boldsymbol{H}_L$ = Hessian of the Lagrangian

I_{yy} = inertia around aircraft y-axis, $\mathrm{kg\,m^2}$

J = cost function

L = Lagrangian

l = lever arm of thrust vector, m

M = big number (representing unboundedness)

$M_{A,y}$ = aerodynamic moment around y-axis, N m

$\boldsymbol{m}_A$ = aerodynamic moment vector, N m

m = aircraft mass, kg

q = pitch rate, $\mathrm{rad\,s^{-1}}$

$\overline{q}_i$ = dynamic pressure at wing i, $\mathrm{N\,m^{-2}}$

$\boldsymbol{R}^{(\dots)}$ = rotation matrix around y-axis

R_p = propeller diameter, m

$\boldsymbol{r}_{wb}$ = relative position between wing and center of gravity, m

S = wing reference area, $\mathrm{m^2}$

s_{sc} = slipstream contraction factor

T = thrust, N

t_0, t_f = initial and final trajectory time, s

u^B, w^B = velocities in body x and z directions, $\mathrm{m\,s^{-1}}$

$\boldsymbol{v}^B$ = velocity vector in body coordinates, $\mathrm{m\,s^{-1}}$

V_x, v_{ax} = axial propeller inflow and propeller induced velocity, $\mathrm{m\,s^{-1}}$

w = weight in cost function

x^E, z^E = horizontal and vertical position in ENU (East-North-Up), m

x_f, z_f = final horizontal and vertical position, m

z, x, u = NLP variable vector, state vector, input vector

z_{ref} = reference altitude, m

$\alpha_{\mathrm{eff}}, \alpha$ = (effective) angle of attack, °

γ = flight path angle, °

δ_w, δ_e = tilt angle and control surface deflection, °

θ = aircraft pitch angle, °

Λ = wing aspect ratio

λ = Lagrange multiplier

ρ = air density, $\mathrm{kg\,m^{-3}}$

τ_k = non-dimensional time in collocation at grid point k

τ_T, τ_{δ_w} = thrust and tilt actuator time constant, s

ϕ_f, ϕ_t = terminal point cost, integral stage cost

ϕ_g, ϕ_b, ϕ_r = path, boundary and rate constraints

$\mathcal{F}_B$ = body frame

$\mathcal{F}_E$ = earth frame (ENU)

$\mathcal{F}_W$ = wing frame

Subscripts

i = index for front (2) and rear (1) wing

A = Aerodynamic

2D, 3D = 2D aerodynamic coefficients, and 3D-corrected coefficients

k = time step on grid

u, l = upper and lower limit

rc = rate constraint

c = commanded value

$0, f$ = initial and final value

Superscripts

B = body frame

W = wing frame

E = ENU frame

I. Introduction

Transformational aircraft promise to combine the advantages of both fixed- and rotary-wing flight, thereby establishing efficient, flexible, and time-saving transport options for poorly connected regions. The subcategory of tilt-wing aircraft provides efficient cruise flight with low requirements on ground infrastructure. As engines and airfoil stay aligned throughout the flight envelope, slipstream effects can be exploited. At the same time, these vehicles show a high complexity compared to other types of the emerging electric vertical takeoff and landing (eVTOL) fleet. Historical challenges arose from complex mechanical control systems [1], bad handling qualities due to the heterogeneous flight envelope [2, 3], and especially restricted design freedom due to fuel-based propulsion [4, 5]. Today, distributed electric propulsion (DEP) allows for flexible vehicle configurations, and recent developments in digitization and automation alleviate limitations of the control system. A remaining challenge is the intuition for and understanding of the flight dynamic behavior, which is characterized by aero-propulsive interactional effects and flow separation. From a flight control perspective, the missing knowledge is circumvented, e.g., in the form of robust [6, 7] or sensor-based [8, 9] control methods. However, a better understanding of the dynamic system is required to derive safe and efficient maneuvers for both nominal and failure cases. In a previous work [10], we developed a representative aircraft model with the ambition to cover all dominant effects. The accompanying static trim analysis provided first insights into the transition behavior but neglected important dynamic characteristics. Therefore, this paper will extend the investigation on tilt-wing transition with a dynamic analysis of different transition strategies, providing insight into the flight dynamic behavior during the crucial transition flight phase.

A. Related Work

Bridging both flight regimes of hover and cruise flight, the transition is the crucial maneuver for tilt-wing aircraft. As these vehicles are not designed for continuous vertical flight, the forward transition (from hover to cruise) is to be performed soon after take-off. In the opposite direction, the backward transition (from cruise to hover) is crucial to enable a safe vertical landing. While the behavior in the regimes of wing-borne and thrust-borne flight resembles other, more familiar aircraft configurations like airplanes, helicopters, and multicopters with well-established theory, the transition regime remains the subject of research. This is, in particular, due to its inhomogeneity with rapidly changing flight conditions. The backward transition is an especially challenging maneuver as the descent flight condition at low thrust settings pushes the effective angle of attack (AoA) towards flow separation [2, 11]. Static trim analyses [10, 12, 13] are often deployed for an initial evaluation and indicate in [10, 12] that flow separation cannot be avoided for level backward transition flight. To avoid flight in post-stall, Fredericks et al. [14] introduce the *zoom* maneuver, which exploits upward aircraft motion during forward and backward transition. By aligning the flight path angle with the wing's attitude, the vertical inflow component in the wing frame is effectively reduced.

To investigate dynamic tilt-wing transition flight without designing a closed-loop controller, optimal control (OC) is commonly deployed. In OC, optimization problems, including continuous system dynamics, are transcribed to nonlinear programming problems (NLP), which can then be solved, for example, using Newton-based solvers [15]. The system dynamics are considered in the form of constraints in the NLP formulation. The OC approach was deployed by Doff-Sotta et al. [16], Chauhan and Martins [17], and Panish and Bacic [18] to optimize transition trajectories for tilt-wing aircraft. These works minimize energy demand during transition or the integral squared thrust as a proxy.

Exploiting a priori knowledge of an Air Traffic Control (ATC) provided flight corridor, [16] reformulates the aircraft equation of motion (EoM) in order to obtain an optimization problem that is convex in objective and constraints. The approach is extended in [19] to model-predictive control (MPC) to form a closed-loop controller. Both works consider slipstream interaction in their modeling approach but otherwise maintain a low complexity, for example, by considering only translational motion in 2D flight path coordinates. Cook [12] identifies dynamic transition trajectories for a pitch-controlled tilt-wing within the level flight manifold without optimization but instead using best guess control policies for the tilt angle to minimize unwanted transition effects.

Besides tilt-wings, transition flight has also been investigated for other types of transformational aircraft, and results and findings can be transferred from there. From a flight mechanics perspective, tailsitter aircraft are particularly comparable to tilt-wing aircraft. Instead of tilting their wings with respect to the fuselage, the pitch attitude of the complete aircraft is changed to convert from hover to cruise flight. Still, this means that (in contrast to, for example, tilt-rotor aircraft) the wing and rotor stay aligned throughout the transition of both tailsitter and tilt-wing, resulting in similar effective angles of attack and aero-propulsive interactions. Compared to tilt-wings, more literature can be found for tailsitter transition analysis, where most investigations likewise use the optimal control approach [20]. While [21] uses a general formulation for the transition, Oosedo et al. [22] optimize for different transition strategies and verify them experimentally. Introducing a constraint to avoid flow separation, [23] creates transitions that exploit vertical aircraft motion to maintain low effective AoA, similar to the strategy proposed in [14] for a tilt-wing aircraft. With the intention of online planning or even control in the form of model predictive control (MPC), [24, 25] use differential flatness properties of the dynamics to reduce the computational cost of the optimization.

B. Scope of the Paper

This paper focuses on the dynamic analysis of the longitudinal tilt-wing transition maneuvers for both forward (from hover to cruise) and backward (from cruise to hover) transition. A setup for trajectory optimization in the form of an optimal control problem formulation is implemented. Based on that, different transition strategies with their respective objectives and constraints are investigated and evaluated. With a focus on manned flight, maneuvers with extreme conditions for pilots and passengers are not considered. Other than that, the intention is to include the most relevant transition strategies.

II. Optimal Control Framework

The developed optimal control framework is primarily based on the guidelines presented by Betts [15] and was extended with insights into the toolboxes FALCON by TUM [26], and ICLOCS2 by Imperial College London [27]. Like both reference toolboxes, the framework is interfaced with the common solver IPOPT [28], which is based on the interior point method. In the following, the dynamic model of the tilt-wing is described first before transferring it to the optimal control formulation.

A. Tilt-Wing Aircraft

The transition analysis is conducted on a tandem tilt-wing configuration as illustrated in Fig. 1. All relevant model parameters are provided in Table 1, with detailed quantitative descriptions given in [10, 29]. The longitudinal motion of the aircraft is of chief interest for the analysis of the transition maneuver. Ignoring failures and lateral wind effects, the aircraft is assumed to be symmetrical with respect to the x-z-plane. Eight propellers and four control surfaces are evenly distributed along both wings and can be summarized in single 2D components. Main (rear) wing components are denoted by index 1, while canard (front) wing components are denoted by index 2. Note that these indices consequently deviate from the notation used in [10, 29], where full 6-degree-of-freedom (DoF) motion was considered. The state of each wing is defined by three inputs, the tilt angle δ_w with a range of $[0°; 90°]$ from level to vertical deflection, the control surface deflection δ_e limited to $[-30°; 30°]$ and the thrust T. In terms of propulsion, the aircraft is controlled by rotor speed, whereas the collective blade pitch is adapted to the different operating states throughout the flight envelope. It is assumed that the maximum thrust of the vehicle equals twice the gravitational force to allow both maneuverability and redundancy in failure cases. Note that this assumption is optimistic, and realistic thrust-to-weight ratios might be significantly lower, depending on the vehicle design. For this work, however, the resulting variable range for T is $[0\,\mathrm{N}; 4500\,\mathrm{N}]$ for the grouped propellers respectively. The index i will be used for wing-dependent variables in the following. While both wings have the same NASA GA(W)-2 profile and a rectangular planform, the reference area of the main wing is larger than that of the canard wing. The center of gravity (CG) is slightly shifted towards the rear section. These design choices characterize the pitching moment behavior during the transition.

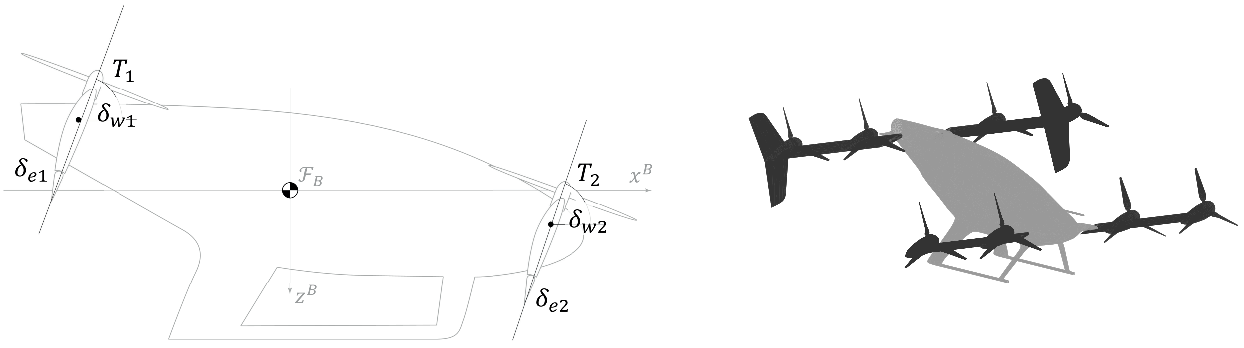

(a)

(b)

Fig. 1 Tandem tilt-wing configuration, (a) sideview in early transition , (b) 3D view in late transition

Table 1 Relevant Tilt-Wing Model Parameter.

Variable	Description	Value
ρ	density	$1.13\,\mathrm{kg\,m^{-3}}$
m	mass	$475\,\mathrm{kg}$
I_{yy}	pitch moment of inertia	$1080\,\mathrm{kg\,m^2}$
R_p	rotor radius	$0.75\,\mathrm{m}$
Λ_1, Λ_2	aspect ratio	6.9, 9.2
c_1, c_2	chord	$0.78\,\mathrm{m}$, $0.57\,\mathrm{m}$
S_1, S_2	surface area	$4.1\,\mathrm{m^2}$, $2.9\,\mathrm{m^2}$
$d_{s,1}, d_{s,2}$	axial distance rotor to wing	$0.52\,\mathrm{m}$, $0.4\,\mathrm{m}$
$l_{1,x}, l_{2,x}$	hor. distance CG to wing	$1.4\,\mathrm{m}$, $2.38\,\mathrm{m}$
$l_{1,z}, l_{2,z}$	vert. distance CG to wing	$0.61\,\mathrm{m}$, $0.47\,\mathrm{m}$

B. Longitudinal Dynamic Model

To keep the number of optimization variables and thereby the size of the resulting NLP problem small, the lateral motion of the aircraft is neglected and a longitudinal model including pitching motion is implemented. The resulting equations of motion can be expressed as:

$$\dot{x}^E = u^B \cos\theta + w^B \sin\theta \tag{1}$$

$$\dot{z}^E = u^B \sin\theta - w^B \cos\theta \tag{2}$$

$$\dot{u}^B = -qw^B - g\sin\theta + \frac{1}{m}\sum_{i=1}^{2}\left(T_i\cos\delta_{w,i} + F^B_{A,x,i}\left(v^B, \delta_{w,i}, T_i, \delta_{e,i}\right)\right) \tag{3}$$

$$\dot{w}^B = qu^B + g\cos\theta + \frac{1}{m}\sum_{i=1}^{2}\left(-T_i\sin\delta_{w,i} + F^B_{A,z,i}\left(v^B, \delta_{w,i}, T_i, \delta_{e,i}\right)\right) \tag{4}$$

$$\dot{\theta} = q \tag{5}$$

$$\dot{q} = \frac{1}{I_{\mathrm{yy}}}\left(\sum_{i=1}^{2} M^B_{A,y,i}\left(v^B, \delta_{w,i}, T_i, \delta_{e,i}\right) + T_i l_i\left(\delta_{w,i}\right)\right) \tag{6}$$

where the aircraft position $\boldsymbol{x}^E = \left[x^E\ z^E\right]^{\mathrm{T}}$ is defined in the ENU frame $\mathcal{F}_E$, while the velocity $\boldsymbol{v}^B = \left[u^B\ w^B\right]^{\mathrm{T}}$ and its derivative is defined in body coordinates $\mathcal{F}_B$ (see Fig. 1(a)). The states for the rotational motion are pitch angle θ and pitch rate q, and the inertia around the y-axis is represented by I_{yy}. The respective thrust forces of main and canard wing have a tilt-angle-dependent lever arm $l_i = f\left(\delta_{w,i}\right)$ to create a control pitching moment. Next to the freestream defined by the body velocity and tilt angle, the thrust-induced slipstream and control surface deflections $\delta_{e,i}$ determine the aerodynamic forces $F^B_{A,x,i}$ and $F^B_{A,z,i}$, and aerodynamic moment $M^B_{A,y,i}$, given in $\mathcal{F}_B$.

For reduced complexity, the rotor model deploys constant thrust and torque coefficients. This assumption is based on a perfect adaptation of the collective blade pitch angle to the axial rotor inflow and the neglect of the lateral inflow component. In addition, the arrangement of counter-rotating propellers, in combination with the symmetry assumption with respect to the x-z plane, results in a cancellation of propeller torque. Therefore, the commanded thrust $T_{c,i}$ is modeled as a direct input.

Concerning aerodynamics and slipstream interactions, the model used for optimization is a simplified form of the strip-theory model presented in [10]. Tandem aerodynamic effects between both wings are neglected, primarily because there exist no generic models that capture the complexity, and reliable data is not available for the considered aircraft configuration. Similarly, the reduction in dynamic pressure due to upstream components (blockage) is not considered. The effect of slipstream interaction is limited to the axially induced velocity, as radial velocities are assumed to cancel due to symmetry. The tangential swirl velocity is neglected to maintain two-dimensional aerodynamics. Further neglecting lateral inflow, the axially induced slipstream velocity [30] is

$$v_{i,\text{ax}} = -\frac{V_{x,i}}{2} + \sqrt{\frac{V_{x,i}^2}{4} + \frac{T_i/4}{2\rho\pi R_p^2}} \tag{7}$$

where $V_{x,i}$ is the inflow velocity perpendicular to the rotor plane. For fully contracted slipstreams, the induced velocity is twice as high as the velocity in the rotor plane [30]. In [6], it was assumed that the aerodynamic reference point is located at the position of full slipstream contraction. As the slipstream contraction model by McCormick [31] is a function of geometry parameters (distance between propeller plane and wing reference point $d_{s,i}$, and propeller radius R_p) which remain constant for the tilt-wing, the induced velocity in the aerodynamic reference point can be represented accurately by a constant slipstream contraction factor $s_{\text{sc},i} < 2$, which is different for both wings:

$$s_{\text{sc},i} = 1 + \frac{d_{s,i}/R_p}{\sqrt{1 + \left(d_{s,i}/R_p\right)^2}} \tag{8}$$

In order to obtain the effective angle of attack α_{eff} at wing i, the effective velocity at the airfoil is calculated by transforming $\boldsymbol{v}^B$ to the wing frame $\mathcal{F}_W$ and adding the slipstream induced velocity:

$$\boldsymbol{v}_i^W = \boldsymbol{R}_i^{WB}\left(\delta_{w,i}\right) \cdot \boldsymbol{v}^B + v_{i,\mathrm{ax}} \cdot s_{sc,i} \begin{bmatrix} 1 & 0 & 0 \end{bmatrix}^{\mathrm{T}} \tag{9}$$

$$\alpha_{\mathrm{eff},i} = \arctan\left(\frac{v_{z,i}^W}{v_{x,i}^W}\right) \tag{10}$$

$$\{C_L, C_D, C_M\}_i = f\left(\alpha_{\mathrm{eff,i}}\right) \tag{11}$$

with the rotation matrix from body to wing frame $\boldsymbol{R}_i^{WB}$. The effect of body rotational rates on the resulting velocity is neglected, as the effect would be small for realistic rates and the pitch motion is balanced to zero within the optimization.

With the effective angle of attack, the aerodynamic coefficients (compare Eq. (11)) can be computed using the model presented by [32], which we adopted in [10]. To improve computational performance, the 360° AoA coefficient model can be preprocessed and saved in look-up tables (LUT). As recommended in [15] for improved convergence, tabular data is interpolated using splines to obtain continuous functions up to second-order derivatives. The effect of control surface deflection on the aerodynamic coefficients is modeled according to [33] and leads to offsets of the aerodynamic coefficients, see Eq. (13) and Eq. (14). However, the control surface model does not capture the change in lift curve slope and stall onset, which are assumed to stay constant. To include the reduced flap effectiveness in post-stall without sacrificing continuity, the offsets due to flap deflections fade out with a scaled arctan-function. Furthermore, an elliptic lift distribution is applied to correct the 2D lift coefficient, resulting in

$$\left(C_{L,\mathrm{3D}}\right)_i = \left(C_{L,\mathrm{2D}}\right)_i \frac{\pi}{4} \qquad \left(C_{D,\mathrm{3D}}\right)_i = \left(C_{D,\mathrm{2D}} + \frac{C_{L,\mathrm{3D}}^2}{\pi\Lambda}\right)_i \tag{12}$$

with aspect ratio $\Lambda_i = {b_i^2}/{S_i}$, b_i and S_i being wing span and wing reference area.

The aerodynamic coefficients are defined in the aerodynamic frame and first need to be transformed to $\mathcal{F}_B$ by applying the rotation matrix $\boldsymbol{R}_y\left(\varphi\right)$ for a rotation around the y-axis. The resulting aerodynamic forces and moments in the body frame are:

$$f_{A,i}^{B} = \overline{q}_i S_i \boldsymbol{R}_y \left(\alpha_{\text{eff,i}} - \delta_{w,i}\right) \begin{bmatrix} -\left(C_{D,\text{3D}} + \Delta C_{D,\delta_e}\right) \\ 0 \\ -\left(C_{L,\text{2D}} + \Delta C_{L,\delta_e}\right) \frac{\pi}{4} \end{bmatrix}_i \tag{13}$$

$$m_{A,i}^{B} = \overline{q}_i S_i c_i \begin{bmatrix} 0 \\ C_M + \Delta C_{M,\delta_e} \\ 0 \end{bmatrix}_i + f_{A,i}^{B} \times r_{wb,i}^{B} \tag{14}$$

Here, c_i is the mean aerodynamic chord and the dynamic pressure is $\overline{q}_i = {}^1\!/\!_2\,\rho ||\boldsymbol{v}_i^W||^2$, while $\boldsymbol{r}_{wb,i}^B$ describes the position of the wing relative to the CG.

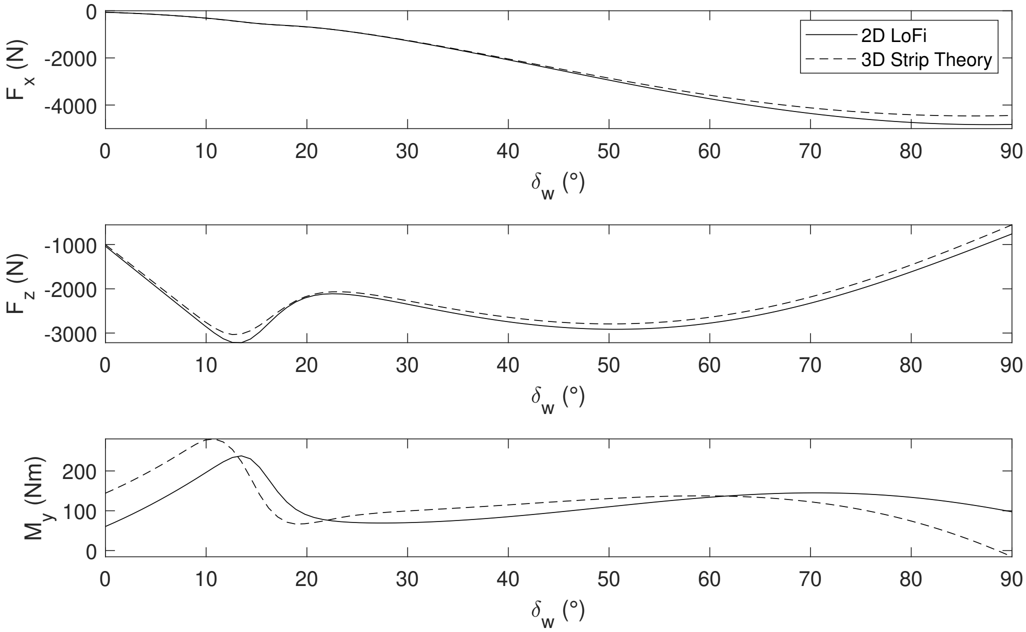

Fig. 2 Comparison of 2D low fidelity and 3D strip theory aerodynamic model for constant axial flight velocity of $V = 25\,\text{m}\,\text{s}^{-1}$ and at constant thrust settings of $T_1 = T_2 = 1500\,\text{N}$.

In order to consider actuator dynamics, system inputs u are modeled as simple transfer functions or by applying lower and upper rate constraints $u_{\text{rc},l}$ and $u_{\text{rc},u}$ in discrete form [15]:

$$u_{\text{rc},l} \leq \frac{u_{k+1} - u_k}{\Delta\tau_k \cdot t_f} \leq u_{\text{rc},u} \tag{15}$$

where the central term describes the change of variable u per discrete time step $\Delta\tau_k \cdot t_f$, with $\Delta\tau_k = (\tau_{k+1} - \tau_k)$ and non-dimensional time at grid point k defined as $\tau_k \in [0, 1]$.

In Fig. 2, the accuracy of this reduced fidelity model for optimal control is compared to the strip theory aerodynamic model presented in [10]. Lateral stabilizers and airfoils on the landing skids, which can be seen in Fig. 1(b)), are neglected in the considered longitudinal models, as their effect is primarily in the lateral direction. Both models show good conformance in the force responses. The trend of the pitching moment is captured with some deviation for cruise and transition flight phases but diverges stronger towards hover conditions ($\delta_w \rightarrow 90°$) and shows a sign reversal. The differences result chiefly from the effect of induced swirl velocity.

C. Optimal Control Problem Formulation

The aim of an optimal control approach is to find the control vector $u(t) \in \mathbb{R}^{n_u}$ that minimizes a cost function $J : \mathbb{R}^{n_x} \times \mathbb{R}^{n_u} \times \mathbb{R} \rightarrow \mathbb{R}$ subject to the dynamics $f : \mathbb{R}^{n_x} \times \mathbb{R}^{n_u} \times \mathbb{R} \rightarrow \mathbb{R}^{n_x}$ of a system with states $x(t) \in \mathbb{R}^{n_x}$ while complying with path, boundary and derivative constraint functions (ϕ_g, ϕ_b and ϕ_r). While path constraints limit output variables $y = g(x, u)$, boundary constraints define the initial and final states $x_0 = x(t_0)$ and $x_f = x\left(t_f\right)$ and the according inputs $u_0 = u(t_0)$ and $u_f = u\left(t_f\right)$. The general mathematical formulation of the problem is

$$\begin{aligned}
\min_{t_f,\, u(t)} \quad & J = \phi_f\left(t_f, x\left(t_f\right), u\left(t_f\right)\right) + \int_{t_0}^{t_f} \phi_t\left(t, x(t), u(t)\right) dt \\
\text{such that} \quad & \dot{x} = f\left(x(t), u(t)\right) \\
& t_l \leq t_f \leq t_u \\
& x_l \leq x(t) \leq x_u \\
& u_l \leq u(t) \leq u_u \\
& g_l \leq \phi_g\left(x(t), u(t)\right) \leq g_u \\
& b_l \leq \phi_b\left(x_0, u_0, x_f, u_f\right) \leq b_u \\
& r_l \leq \phi_r\left(x(t), u(t)\right) \leq r_u
\end{aligned} \tag{16}$$

where ϕ_f represents the terminal point cost and ϕ_t is the integral cost, usually used in squared form. The initial time t_0 is fixed to zero, while the terminal time t_f is free and part of the optimization problem. Subscripts u and l indicate upper and lower limits, respectively.

The system dynamics are enforced as collocation defects $\boldsymbol{c}_d$ (state integration errors on the collocation grid). To ensure valid system dynamics, all defects must be zero, which results in the additional constraints $\boldsymbol{c}_d = 0$. The full constraint vector contains the collocation defects, as well as path, boundary, and rate constraints:

$$\boldsymbol{c} = \left[\boldsymbol{c}_d, \phi_g, \phi_b, \phi_r\right] \tag{17}$$

with upper and lower limits $\boldsymbol{c}_l \leq \boldsymbol{c} \leq \boldsymbol{c}_u$.

To solve the problem with Newton-based methods on a finite set of variables and constraints, the continuous problem is transcribed using a direct collocation method to obtain an NLP. Here, direct collocation with the trapezoidal method on a grid with N points is applied. The resulting NLP variables to be optimized are:

$$\boldsymbol{z} = \left[t_f, x_1, u_1, x_2, u_2, \ldots, x_N, u_N\right]^{\mathrm{T}} \tag{18}$$

where the indices $k = 1, ..., N$ correspond to the respective time grid points. The resulting variable time step is a function of terminal time $\Delta t = \frac{t_f}{N-1}$. Eq. (18) shows that the size of the NLP depends on the number of inputs and states describing the dynamic system as well as the temporal discretization. The form of the variable vector $\boldsymbol{z}$ exploits the sparsity pattern of the Jacobian $\boldsymbol{G} \equiv \frac{\partial \boldsymbol{c}}{\partial \boldsymbol{z}}$ and the Hessian of the Lagrangian

$$\boldsymbol{H}_L = \nabla^2_{zz} L(z) = \nabla^2_{zz} J(z) - \sum_{i=1}^{m} \lambda_i \nabla^2_{zz} \boldsymbol{c}_i(z) \tag{19}$$

with Lagrange multipliers λ_i, as explained in [15]. Further methods applied to improve accuracy and convergence are scaling of variables and a remesh strategy.

Transferred to the tilt-wing 3-DoF application, the state and input vectors, according to Section II.B, are:

$$\boldsymbol{x} = \begin{bmatrix} x^E & z^E & u^B & w^B & \theta & q & T_1 & T_2 & \delta_{w1} & \delta_{w2} \end{bmatrix}^{\mathrm{T}} \tag{20}$$

$$\boldsymbol{u} = \begin{bmatrix} T_{1,c} & T_{2,c} & \delta_{w1,c} & \delta_{w2,c} & \delta_{e1,c} & \delta_{e2,c} \end{bmatrix}^{\mathrm{T}} \tag{21}$$

Here, the inputs of thrust T and tilt angle δ_w were modelled as first-order delay elements (time constants $\tau_T = 1/5$ and $\tau_{\delta_w} = 2$). This introduces additional states to the problem and thus increases the complexity. Nevertheless, capturing the correct dynamics of tilt actuation and thrust is considered essential for realistic trajectories. In contrast, control surface deflections (δ_e) are responsive and thus are only rate-limited according to Eq. (15) as a compromise between complexity and accuracy. Table 2 gives an overview of nominal variable bounds and rate constraints. Single variables are then adapted to the respective transition strategy. The constant M is an appropriately large number that represents unboundedness. Maximum accelerations in $\mathcal{F}_B$ are given as ratios of gravitational acceleration g and are adopted from values for nominal takeoff and landing maneuvers of commercial airliners. In addition to the first-order delay behavior of thrust and tilt angle, the commanded inputs are smoothed using additional rate constraints. As the exploration space of the IPOPT solver is not hard-limited by the variable boundaries, the lower bound for the thrust is increased from 0 to 1 to avoid complex results in Eq. (7).

The optimized transition trajectory leads the aircraft from hover (x_h) to cruise (x_c) conditions or vice versa. Considering the state variables, the hover flight state is defined by zero body velocities $u^B = w^B = 0$ and a high tilt angle

Table 2 State and input variables of the optimal control problem and their respective boundaries and rate constraints.

State Variables					
Variable	Unit	lower Bound	upper Bound	lower Rate Constraint	upper Rate Constraint
x^E	m	0	M	0	100
z^E	m	$-M$	M	−50	50
u^B	$\mathrm{m\,s^{-1}}$	0	100	$-0.5g$	$0.5g$
w^B	$\mathrm{m\,s^{-1}}$	−50	50	$-0.25g$	$0.25g$
θ	°	−0.5	0.5	$-M$	M
q	$^\circ\,\mathrm{s^{-1}}$	−0.01	0.01	$-M$	M
T_1	N	1	4500	$-M$	M
T_2	N	1	4500	$-M$	M
$\delta_{w,1}$	°	0	90	$-M$	M
$\delta_{w,2}$	°	0	90	$-M$	M
Input Variables					
Variable	Unit	lower Bound	upper Bound	lower Rate Constraint	upper Rate Constraint
$T_{1,c}$	N	1	4500	$-M$	M
$T_{1,c}$	N	1	4500	$-M$	M
$\delta_{w1,c}$	°	0	90	−45	45
$\delta_{w2,c}$	°	0	90	−45	45
$\delta_{e1,c}$	°	−30	30	−45	45
$\delta_{e2,c}$	°	−30	30	−45	45

$\delta_{w,i,\text{hover}} = \{\delta_{w,i} \mid 80^\circ \le \delta_{w,i} \le 90^\circ\}$, while cruise conditions entail zero vertical velocity $w^B = 0$ but a horizontal velocity $u^B_{\text{cruise}} = \{u^B \mid 40\,\mathrm{m\,s^{-1}} \le u^B \le 50\,\mathrm{m\,s^{-1}}\}$ and low tilt angle $\delta_{w,i,\text{cruise}} = \{\delta_{w,i} \mid 0^\circ \le \delta_{w,i} \le 10^\circ\}$. Note that in contrast to conventional aircraft, the wing AoA can be controlled via wing tilt angle next to the aircraft's vertical motion and pitch angle. This allows limiting the pitch angle to values close to 0°, see Table 2. Other variable bounds are either consistent with Table 2 or depend on the considered transition strategy. The respective flight states are assigned to the initial and terminal state conditions x_0 and x_f according to the transition direction. The initial and final inputs are found with a trim analysis, $\boldsymbol{u}_0 \in \{\boldsymbol{u} | \dot{\boldsymbol{x}}\,(t_0, \boldsymbol{u}) = 0\}$ and $\boldsymbol{u}_f \in \left\{\boldsymbol{u} | \dot{\boldsymbol{x}}\,\left(t_f, \boldsymbol{u}\right) = 0\right\}$, enforcing both hover and cruise to be equilibrium flight states. In [18], the importance of the initial guess solution for convergence is highlighted. For the presented setup, it was sufficient to interpolate between initial and final trim state to obtain initial guesses on the discrete time grid. However, this setup solves a sequence of optimal control problems with increasing complexity and forwarding the solution from one stage to the next. A simple model, neglecting flaps and first-order delay behavior of inputs, is solved first before the presented "full" problem is warm-started with that solution. This improves computation time, while the standalone "full" problem can likewise be solved directly. A similar positive effect on computation time is observed when the problem is initially solved on a coarse grid and mesh refinement is applied subsequently. Final results are obtained on a grid with $N = 101$ control points.

In general, the following objectives are of interest for the optimization of transition trajectories:

- minimize the transition time t_f, as flight within the thrust-based flight regime is energy-demanding
- minimize the terminal distance x^E_f, for transition maneuvers in tight spaces
- minimize the terminal altitude z^E_f, especially for backward transition, as vertical descent is energy-demanding
- minimize the error from a reference trajectory, defined by z_{ref}, for level or glide-path transitions

which results in the following multi-objective cost function.

$$J = w_1\, t_f + w_2\, x^E_f + w_3\, z^E_f + \int_0^{t_f} \left[w_4 \left(z^E - z^E_{\text{ref}} \right)^2 \right] dt \tag{22}$$

The weights w_j determine the user-defined importance of single objectives but are also used to scale all terms to a value close to unity to obtain a well-posed Hessian matrix.

In this work, the objective function expressed in Eq. (22) primarily serves to enforce a certain transition strategy, as will be presented in detail in Section III. For future applications, this could be extended or replaced by other optimization criteria like energy or noise. However, this requires adapting the model accordingly.

III. Transition Strategies

In this section, different strategies for performing the transition maneuver are explained, described mathematically in the form of constraint and cost functions, and discussed with respect to the optimization results. Only appropriate options for manned flight are considered, which yields three main conversion maneuvers. First, the initial altitude is maintained. Second, an upward motion of the aircraft can be exploited to positively affect the AoA, thereby avoiding flow separation. The last option is the opposite and consequently includes a downward motion, which initially sounds counterintuitive, as that further increases the AoA.

A. Level Transition

The level transition maintains the initial altitude z^E throughout the maneuver, leading to $\dot{z}^E = 0$. It is a typical reference case for static trim analysis [12, 34], allowing a simple initial examination of transition characteristics. Without a vertical velocity component, high effective AoA are usually encountered during the transition, and flow separation occurs. This is more severe for backward transition maneuvers, as the thrust setting is low and the effect of the slipstream is small. The post-stall flight regime is characterized by its non-linearity, wherefore trim points are not unique when crossing the stall boundary, and the tilt angle trajectory takes the shape of an "S"-curve or fold. This effect was discovered in 1968 by Kirkpatrick and Murphy[34] in the course of static wind-tunnel investigations (see Fig. 3(b)), and was reproduced independently in previous work [10] (compare Fig. 3(a)) and by Cook[12]. The occurrence of the fold in the tilt-angle range depends on the selected airfoil and its respective stall onset. It implies the aircraft would decelerate in an accelerated conversion maneuver, and vice versa. This is not only counterintuitive but also uncomfortable for pilot and passengers. According to [34], the effect can be reduced by deploying stall-delaying airfoils or control surfaces acting like high-lift devices. Furthermore, the author in [34] mentions that the transition fold is not encountered or at least strongly decreased in the course of flight tests. That is primarily due to inertial effects in dynamic transitions, which were neglected in the trim studies. One motivation for this work is to see whether the same result can be obtained in a dynamic analysis using the optimal control approach. If this is confirmed, it would suggest that the simple trim analysis can be misleading in terms of tilt-wing flight characteristics.

Still, the static trim lines in Fig. 3(a) indicate a general trend. With increasing acceleration, the region of non-linear behavior becomes smaller, meaning that the forward transition maneuver is good-natured. In contrast, the non-linearities increase for higher decelerations during the backward maneuver, and there is a region between $30\,\mathrm{m\,s^{-1}}$ to $40\,\mathrm{m\,s^{-1}}$ where no trim solutions are found. This might be an indicator of difficult transition flight conditions.

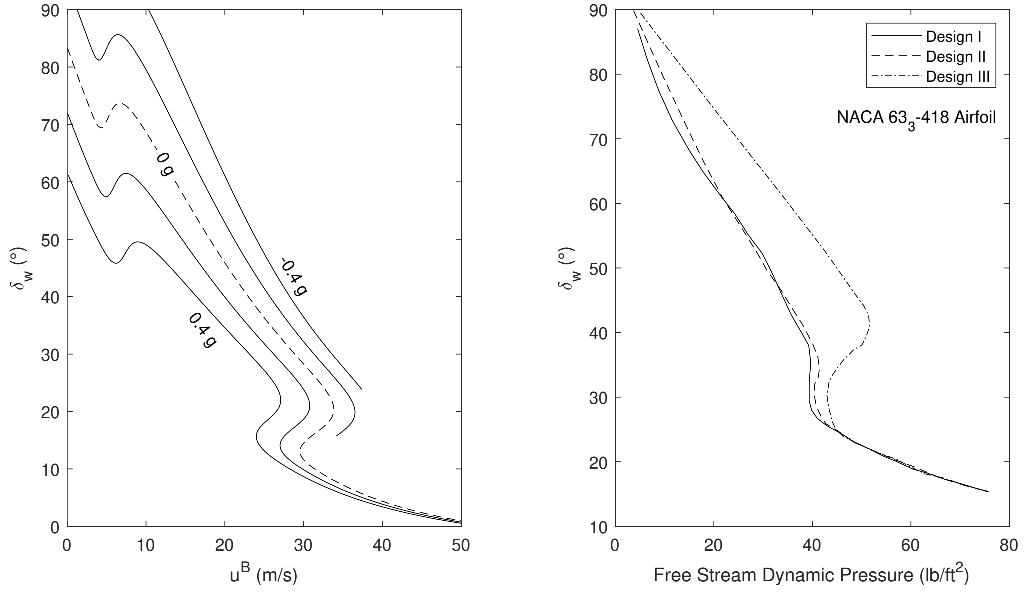

(a) Trim trajectories for different horizontal accelerations

(b) Trim results for different wing designs, from [34]

Fig. 3 Comparison of transition trajectories with characteristic fold, for simulation-based tandem tilt-wing (a) and wind-tunnel-based single wing trim studies (b).

Instead of strictly limiting the vertical motion by adapting variable and rate boundaries in Table 2, an upward motion ($0 \leq z^E$, $0 \leq \dot{z}^E$) is allowed to avoid too hard constraints for the optimization. Instead, the cost function enforces the level transition, with $w_2 = w_3 = 0$ in Eq. (22). The reference altitude is replaced with the initial altitude z_0^E. The solver is capable of minimizing the integral squared vertical displacement to the order of 10^{-7}. If only the vertical offset is considered as objective, longer transition times do not significantly impact the cost function, and the solution runs to the upper limit of the terminal time. Therefore, t_f is preserved in the cost function, but with $w_1 \ll w_4$.

$$J = w_1\, t_f + \int_0^{t_f} \left[w_4 \left(z^E - z_0^E \right)^2 \right] dt \tag{23}$$

$$w_1 = 1\ ,\ w_4 = 100 \tag{24}$$

Forward The resulting trajectory is shown in Fig. 4. In the upper plot, the black arrow represents the sum of the aerodynamic and propulsive force vectors, which accelerates the vehicle in the horizontal direction while balancing the gravitational vertical force. As can be seen, the initial and terminal force vectors are purely vertical with the magnitude of the gravitational force, as these states are trimmed. In the second plot, arrows represent the attitude of both wings. To better illustrate the difference between both wing tilt angles, both arrows share the same origin in the vehicle's CG. While the canard tilt angle is higher in trimmed hover conditions (at $x^E = 0$), it passes the main wing's position in early transition and leads the transition maneuver, until the main wing tilt angle catches up in late transition. This is also visualized in Fig. 5(a). The behavior is due to the altered lever arms and their impact on the pitching moment as a function of tilt angle.

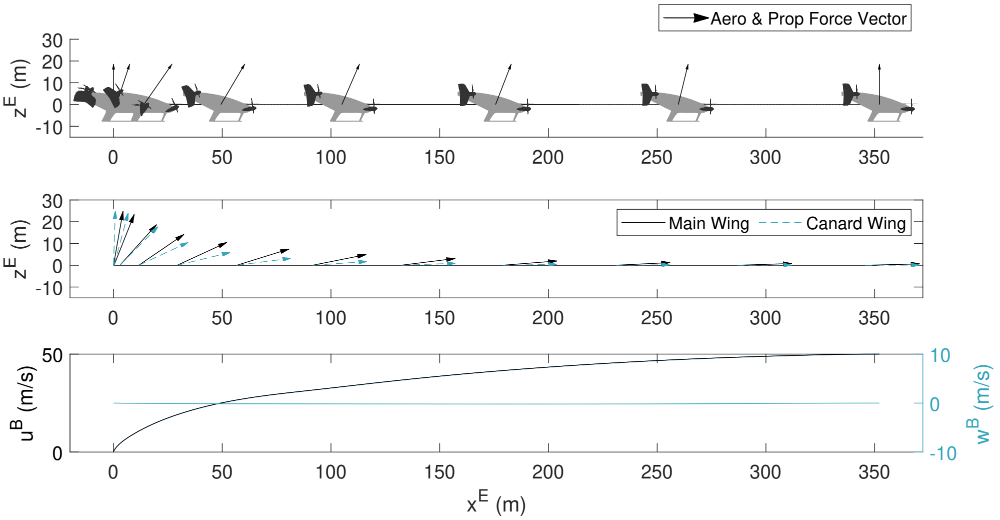

Fig. 4 Trajectory and velocities of level forward transition

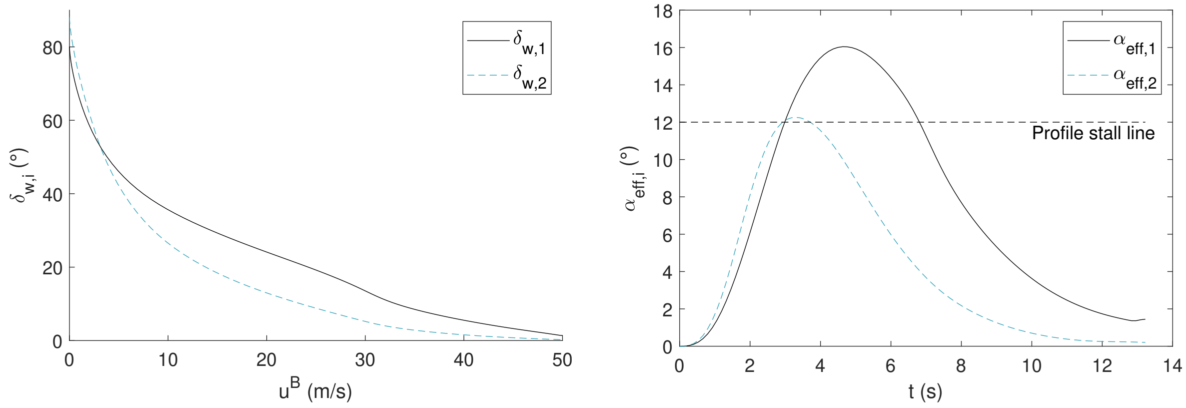

(a) Tilt angle trajectory

(b) Effective angles of attack

Fig. 5 Transition tilt angle trajectory and effective angles of attack for forward level transition.

The last plot in Fig. 4 shows the aircraft velocities in the body frame, corresponding to the NED-frame for zero pitch. As intended, the vertical velocities are 0 while the horizontal velocity increases smoothly with ongoing transition.

As we were interested in the dynamic behavior in nonlinear post-stall, the resulting transition trajectory is transferred to the same plot as in Fig. 3(a), where the tilt angle is plotted over flight velocity. This corresponds to the definition of the tilt-wing transition corridor, and the plots thus give insides on the chosen path through the corridor during the transition. Fig. 5(a) shows that, in comparison to the trim case, no transition fold is encountered. While there is a weak hump in $\delta_{w,1}$ at around 30°, $\delta_{w,2}$ stays smooth. The latter can be explained by Fig. 5(b), which shows that the canard wing does not encounter severe flow separation, as the maximum of $\alpha_{\text{eff},2}$ stays close to $\alpha_{\text{stall}} = 12°$ (indicated by the dashed horizontal line). That is due to the lower tilt angle of the canard wing, see Fig. 5(a). In contrast, the main wing crosses into the post-stall regime. Still, the fold that was observed for trimmed flight is damped out. This confirms that the results from the static trim analysis on the tilt-wings' transition behavior should be reviewed with care, as the dynamic behavior could be significantly different.

As explained above and shown in [6], forward acceleration has a positive effect on the transition characteristics, wherefore the more meaningful analysis is on the backward transition.

Backward Compared to the forward case, the solution for level backward transition requires a larger horizontal distance to perform the maneuver as the deceleration capabilities of tilt-wings are limited [35]. The relative motion of the tilt angle for the backward case, shown in Fig. 6 and Fig. 7(a), is very similar to that of the forward case. For low velocities $\delta_{w,1} < \delta_{w,2}$ holds, which is reversed for high velocities. As predicted by the trim analysis Fig. 3(a), decelerations push the tilt angle trajectories to higher values than the forward transition.

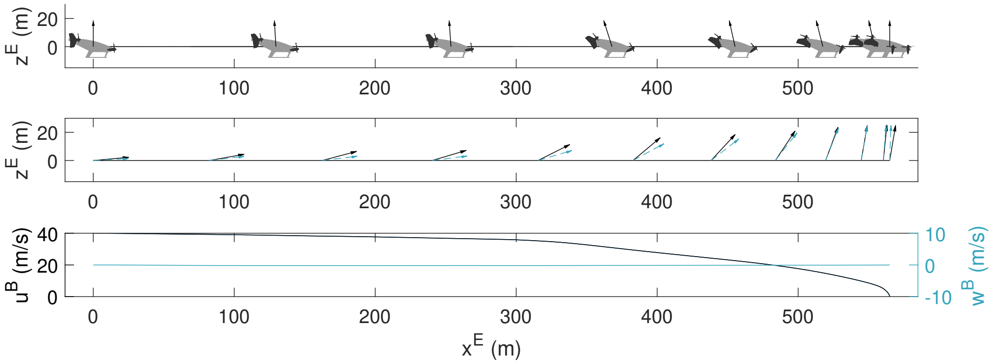

Fig. 6 Trajectory and velocities of level backward transition

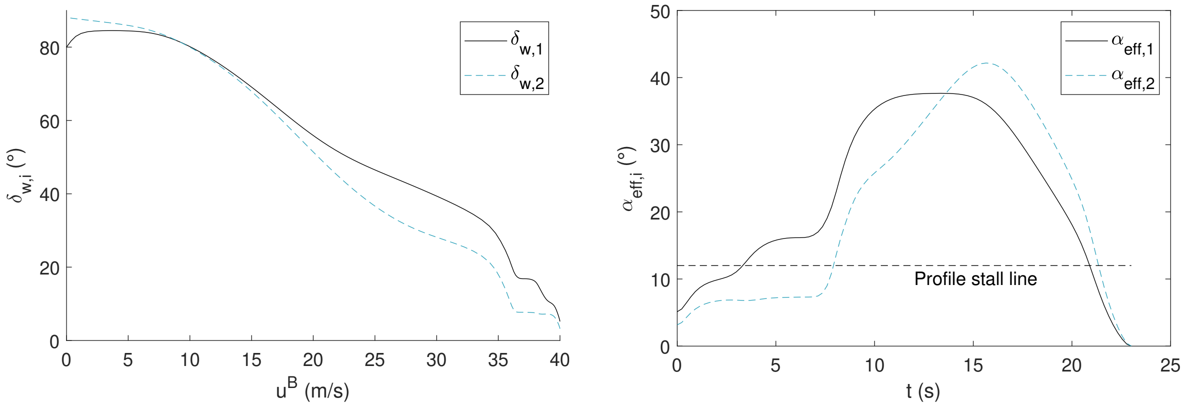

(a) Tilt angle trajectory

(b) Effective angles of attack

Fig. 7 Transition tilt angle trajectory and effective angles of attack for backward level transition.

The decelerating maneuver dictates low thrust settings, which result in larger effective AoA (compare Fig. 7(b)). Consequently, both wings enter deeply into the post-stall region, particularly in early backward transition which is between approximately $32\,\mathrm{m\,s^{-1}}$ and $40\,\mathrm{m\,s^{-1}}$. This introduces non-linearities to the tilt angle trajectories in Fig. 7(a), which occur when crossing the fold in Fig. 3(a) from linear AoA range to post stall conditions. This shows that the static analysis helps to identify regions of the flight envelope with challenging transition conditions. Despite the non-linearities, the curves for both tilt angles are still monotonic and a continuously decelerating maneuver can be observed in the velocity plot. It is also apparent that deceleration capabilities are improved once the hump at $u^B = 35\,\mathrm{m\,s^{-1}}$ in Fig. 7(a), corresponding to $x^E \approx 300\,\mathrm{m}$ in Fig. 6, is passed. Nevertheless, note that flight in post-stall can introduce severe buffeting, which might lead to comfort issues or induce high structural loads.

B. Transition without Flow Separation

Depending on aircraft and airfoil, the onset of stall is often accompanied by large fluctuations (buffeting), while the resulting aerodynamic coefficients in [32] (used in Eq. (11)) represent an averaged result in this AoA range. Strong fluctuations of aerodynamic forces put stress on crew, passengers, and aircraft structure and might also impair flight stability. Therefore, transformational aircraft often try to avoid flight in the post-stall regime [2] by loosening the vertical velocity constraint [14]. Within the optimal control framework, path constraints for the effective AoA are introduced:

$$\alpha_{\text{eff},i} < \alpha_{\text{stall}} \tag{25}$$

Upward aircraft motion is usually exploited to avoid flow separation. This can be included in the constraints by restricting $\dot{z}^E$ to always be positive. It was already mentioned that a large increase in altitude during transition is undesired, especially for the backward case. For forward transition, however, upward motion can be desired during transition to initiate the climb phase. Nevertheless, we gain more insight by focusing on the boundary case and, therefore penalize the terminal altitude within the cost function for both forward and backward transition:

$$J = w_1 \, t_f + w_3 \, z_f^E \tag{26}$$

$$w_1 = 1 \,, \; w_3 = 0.01 \tag{27}$$

Forward The results show that the aircraft is capable of satisfying both level and flow separation constraints, and the resulting trajectory looks similar to the results obtained in Fig. 6. It is, therefore, not shown. Instead, we are more interested in the differences between the two cases. For the level transition, the effective angles of attack only moderately exceed the stall boundary, so slight modifications of actuator inputs are sufficient to prevent flow separation.

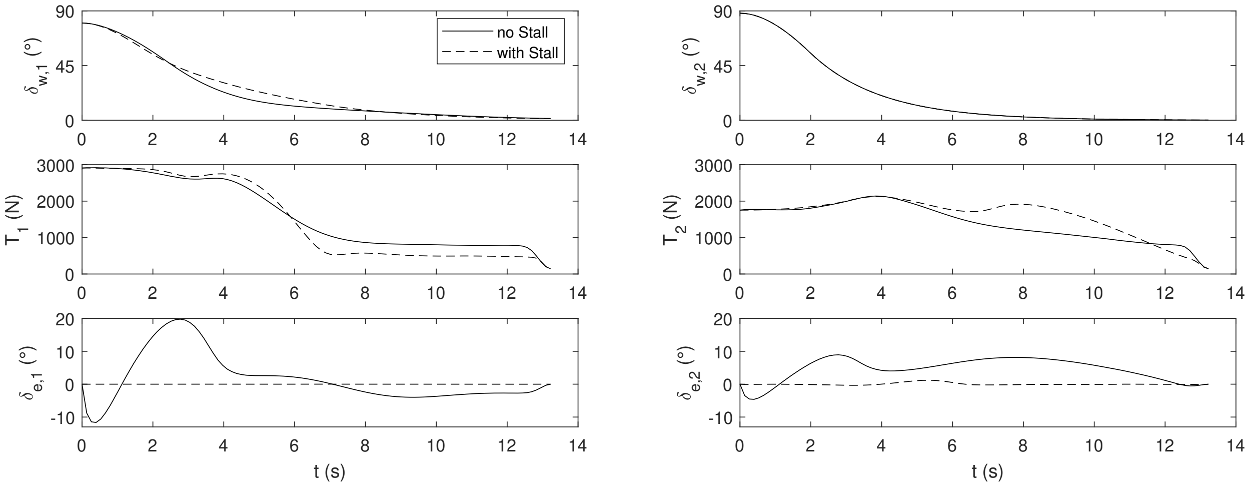

(a) Main Wing

(b) Canard Wing

Fig. 8 Comparison of actuator inputs at both wings, with and without flow separation prevention

A comparison between level forward transition with and without flow separation is given for thrust and tilt angle in Fig. 8.

While the canard tilt angle stays almost unchanged, the main wing tilt angle is reduced within the time span from 3 to about 8 s, where stall occurred for the level maneuver (compare Fig. 5(b)), in order to reduce the effective AoA. A combination of control surface deflection and differential thrust compensates for the change in tilt angle. In comparison to the level case, where control surfaces are hardly deployed, significant deflections are required particularly on the main wing. Fig. 9 shows that the effective angle of attack stays below the stall angle of attack, suggesting that flow separation is successfully avoided. This leads to a smoother tilt angle trajectory when compared to the level case.

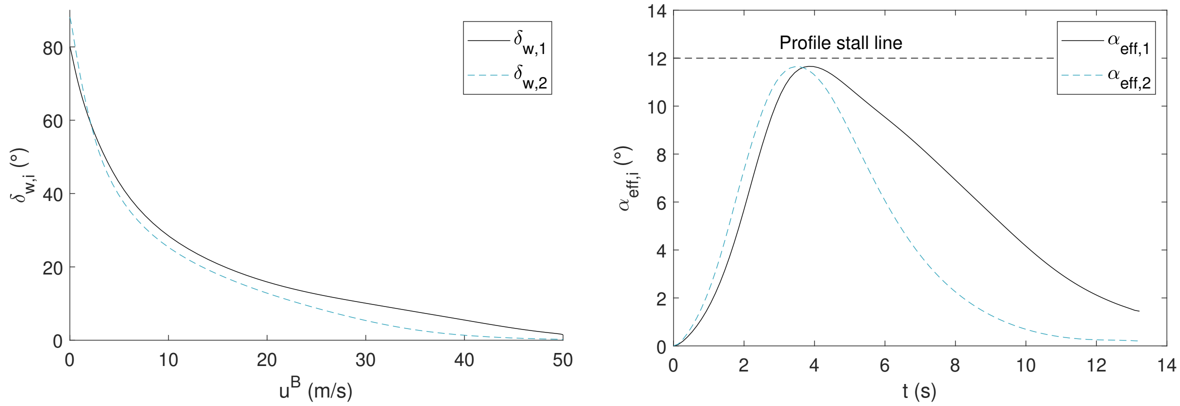

(a) Tilt angle trajectory

(b) Effective angles of attack

Fig. 9 Transition tilt angle trajectory and effective angles of attack for forward transition without flow separation.

Backward While a forward level transition was possible without flow separation, the backward transition requires an upward motion to reduce the effective angle of attack, see Fig. 10, if flow separation is to be avoided. The conversion of kinetic to potential energy can be exploited to achieve short backward transitions when comparing final time and distance with the level case.

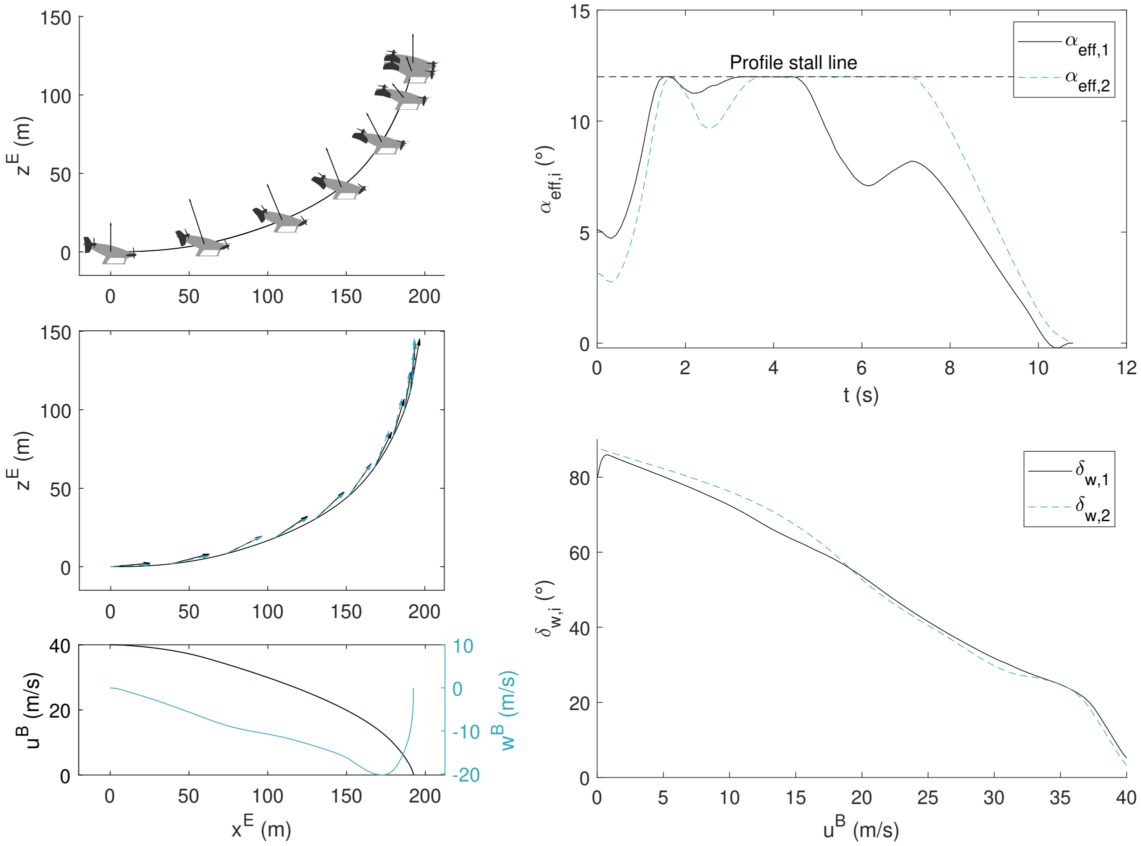

Fig. 10 Results for backward transition without flow separation.

The total aerodynamic and propulsive force acts as a centripetal force that causes a circular upward motion, as shown in the upper left plot in Fig. 10. In late backward transition, the force vector is tilted to the left, which leads to a strong deceleration of both upward (due to gravitation) and forward motion. The center-left plot illustrates the idea behind transition maneuvers avoiding flow separation: To reduce the effective AoA, the tilt angle deflection is kept almost tangential to the flight path. That explains why both tilt angle deflections take similar trajectories in the lower right plot until assuming the differential tilt configuration for trimmed hover flight at $u^B = 0$. Comparing this plot with the result for the level transition, the desired smoothing effect in the tilt angle trajectory is observed. The AoA plot in Fig. 10 indicates that the effective angle of attack stays below the profile stall line.

C. Dive & Glide Path Transition

The previous cases demonstrated that an upward motion can effectively reduce the AoA and avoid stall. In contrast, this section investigates the effect of downward aircraft motion during the transition phase.

Dive Transition The dive transition exploits the conversion of potential to kinetic energy to quickly gain velocity in forward transition. A loss in altitude is accepted, wherefore the vertical force provided by airfoils and thrust is not required to balance gravity. From an optimal control perspective, the state boundaries in Table 2 are adapted to allow only a downward motion. It was already observed for the backward transition with upward motion in Fig. 10 that the shortest transitions can be achieved when exploiting energy conversion. To enforce a dive transition, the terminal time is set as a single objective (similar results are obtained when minimizing the terminal distance).

$$J = w_1\, t_f \;,\; w_1 = 1 \tag{28}$$

As shown in Fig. 11, the cost function successfully triggers the desired behavior, and the aircraft descends more than 80 m throughout the maneuver. Without having to create sufficient lift to balance gravity, the aircraft is allowed to rapidly tilt both wings downwards. This results in a large acceleration in both downward and forward direction. With rising flight speed, aerodynamic forces become dominant and the aircraft quickly transitions from thrust- to wing-borne flight. As expected, the dive trajectory results in a severe increase of effective AoA (Fig. 12).

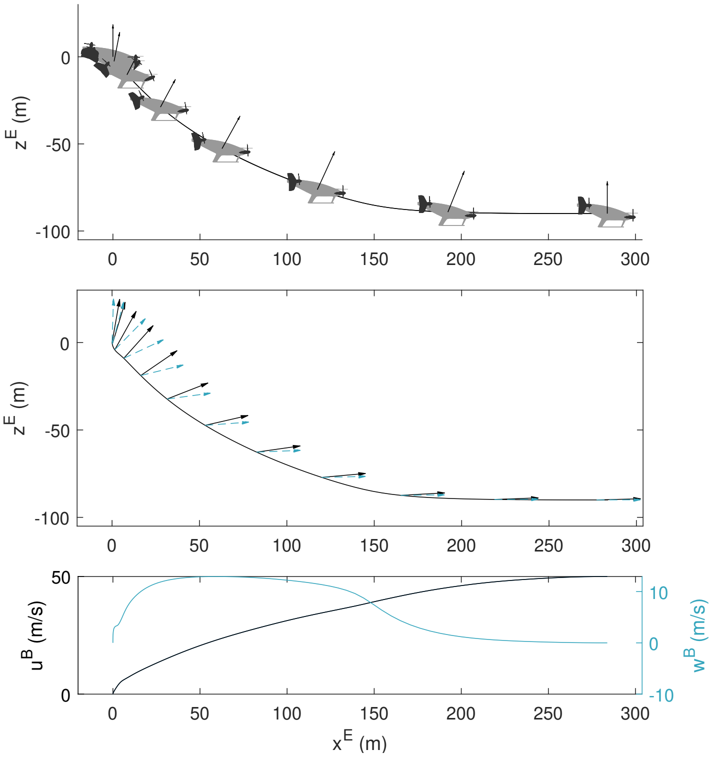

Fig. 11 Trajectory and velocities of dive transition

Glide Path Conventional aircraft follow a glide path when approaching the runway. To reflect possible ATC requirements, a similar operation is considered in the form of the glide path transition. This represents the most challenging maneuver for common tilt-wing flight [2]. Not only does the downward motion increase the AoA, but at the same time, the propellers are close to idle (to allow deceleration), which reduces the positive slipstream effect on the

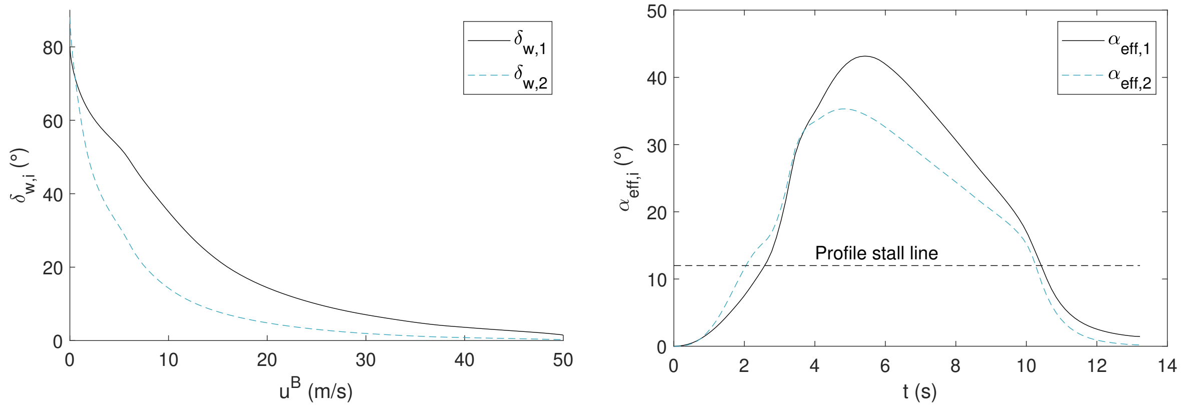

(a) Tilt angle trajectory (b) Effective angles of attack

Fig. 12 Transition tilt angle trajectory and effective angles of attack for dive transition.

effective AoA. In addition, the conversion of potential to kinetic energy along the glide path counteracts the desired decelerating maneuver. The strategy can be imposed by penalizing deviation from a commanded glide path, represented by reference altitude z^E_{ref} in the cost function:

$$J = \int_0^{t_f} w_4 \left(z^E - z^E_{\text{ref}}\right)^2 dt \tag{29}$$

$$w_4 = 1/t_f \tag{30}$$

where the reference altitude is a function of the current horizontal position:

$$z^E_{ref} = z^E_0 - \left(x^E - \Delta x^E\right) \cdot \tan\gamma \tag{31}$$

with initial altitude z^E_0 and glide path angle γ. The "fade-in" distance Δx^E allows the aircraft to intercept the glide slope. Here, $\Delta x^E = 500\,\text{m}$, $z^E_0 = 100\,\text{m}$ and $\gamma = 15°$ were chosen. Although aircraft approaches are usually conducted at angles of about 3°, the high value for the path angle was chosen for better visualization of the trajectory (and because the vehicle is capable of flying such a maneuver). To avoid climbing within the fade-in distance, an upward motion of the aircraft is restricted by variable constraints.

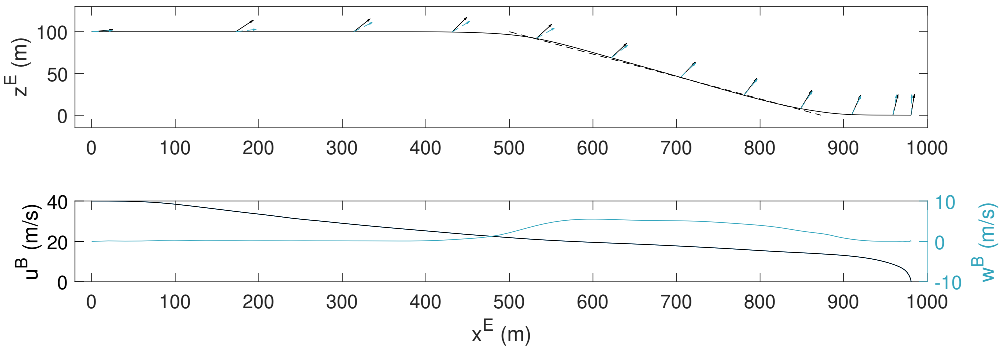

Fig. 13 Trajectory and velocities of glide path transition

Aiming at good tracking of the prescribed path, the influence of time on the objective is canceled by choosing $w_4 = {}^1/_{t_f}$, see Eq. (30). Otherwise, the solver minimizes the flight time instead of accurately tracking the glide path.

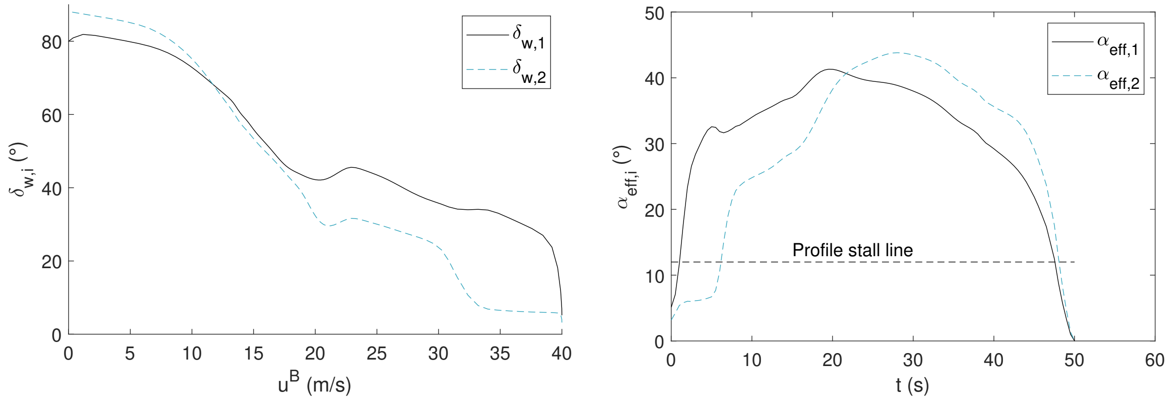

(a) Tilt angle trajectory

(b) Effective angles of attack

Fig. 14 Transition tilt angle trajectory and effective angles of attack for glide path transition.

The resulting trajectory is shown in Fig. 13, with the glide path being represented by a dashed line. It is interesting to see that a strong deceleration is initiated by an upward motion of the main wing within the fade-in distance. In this flight regime, both tilt wings show very different tilt angles and the angles' trajectories are not monotonic (Fig. 14(a)). Fading into the glide slope, the aircraft already reduced its velocity by a factor of 2. On the glide path, both tilt angles align, and the aircraft can still decelerate horizontally. However, the gradient of u^B is smaller on the glide path compared to the fade-in distance. Fig. 14(b) confirms that this maneuver is undesirable from an aerodynamics point of view, as both wings are in post-stall throughout most of the transition.

IV. Conclusion

This paper investigates tilt-wing transition flight using an optimal control approach. The presented setup for trajectory optimization allows for increased model complexity compared to similar approaches, encompassing non-linear aerodynamics, propeller wing interaction, and relevant actuator dynamics. Despite a large number of optimization variables and strong non-linearities, the framework still shows robust convergence without dependency on expensive initialization procedures. In this work, different longitudinal transition strategies are enforced by adapting the constraints and objectives of the problem formulation. It is shown that strong non-linearities due to flow separation, occurring in static transition trim investigations, are attenuated significantly in this analysis due to inertial effects, thereby highlighting the relevance of dynamic investigations. Furthermore, the backward transition from cruise to hover conditions proves to be the critical maneuver due to the unfavorable combination of low thrust settings and high angles of attack. The considered strategies show that flow separation during backward transition can only be avoided with an upward aircraft motion, which is counter-productive regarding energy consumption and counter-intuitive for pilot and air traffic control. In contrast, the effective angle of attack is even further increased when following a conventional glide path. This could, therefore, be a potential showstopper for the tilt-wing aircraft and suggests that flight in post-stall conditions has to be accepted for this type of aircraft. In general, the developed framework supports a better understanding of aerodynamics and flight dynamics within a tilt-wing's transition flight phase, which is a valuable contribution to the fields of vehicle design, flight control, and flight guidance.

References

[1] Phillips, F. C., "The Canadair CL-84 Tilt-Wing V/STOL Programme," *The Aeronautical Journal*, Vol. 73, No. 704, 1969, pp. 713–723. https://doi.org/10.1017/S0001924000052003.

[2] Michaelsen, O. E., and Martin, J. F., "The Aerodynamic Approach to Improve Flying Qualities of Tilt-Wing Aircraft," *9th Anglo-American Aeronautical Conference*, 1963. https://doi.org/10.2514/6.1963-484.

[3] Breul, H. T., "A Simulator Study of Tilt-Wing Handling Qualities," *Heterogeneous Combustion Conference*, AIAA, 1963. https://doi.org/10.2514/6.1963-1015.

[4] Josephs, L. C., and Hesse, W. J., "Survey of Significant Technical Problems Unique to VSTOL Encountered in the Development of the XC-142A," *Journal of Aircraft*, Vol. 3, No. 1, 1966, pp. 3–10. https://doi.org/10.2514/3.43699.

[5] Gaebe, H. M., "Some Important Design Considerations on the XC- 142A Triservice VSTOL," *Journal of Aircraft*, Vol. 2, No. 1, 1965, pp. 9–12. https://doi.org/10.2514/3.43611.

[6] Cook, J., and Hauser, J., "A Strip Theory Approach to Dynamic Modeling of eVTOL Aircraft," *AIAA SciTech 2021 Forum*, AIAA, 2021. https://doi.org/10.2514/6.2021-1720.

[7] Panza, S., Lovera, M., Sato, M., and Muraoka, K., "Structured μ-Synthesis of Robust Attitude Control Laws for Quad-Tilt-Wing Unmanned Aerial Vehicle," *Journal of Guidance, Control, and Dynamics*, Vol. 43, No. 12, 2020, pp. 2258–2274. https://doi.org/10.2514/1.g005080.

[8] Milz, D., and Looye, G., “Tilt-Wing Control Design for a Unified Control Concept,” *AIAA SciTech 2022 Forum*, AIAA, 2022. https://doi.org/10.2514/6.2022-1084.

[9] Binz, F., Islam, T., and Moormann, D., “Attitude Control of Tiltwing Aircraft Using a Wing-Fixed Coordinate System and Incremental Nonlinear Dynamic Inversion,” *International Journal of Micro Air Vehicles*, Vol. 11, 2019. https://doi.org/10.1177/1756829319861370.

[10] May, M. S., Milz, D., and Looye, G., “Semi-Empirical Aerodynamic Modeling Approach for Tandem Tilt-Wing eVTOL Control Design Applications,” *AIAA SciTech 2023 Forum*, AIAA, 2023. https://doi.org/10.2514/6.2023-1529.

[11] Deckert, W. H., Page, R. V., and Dickinson, S. O., “Large-Scale Wind-Tunnel Tests of Descent Performance of an Airplane Model with a Tilt Wing and Differential Propeller Thrust,” Tech. Report TN D-1857, NASA, Washington, D.C., Oct. 1964.

[12] Cook, J. W., “Exploration of Dynamic Transitions of Tiltwing Aircraft Using Differential Geometry,” Ph.D. thesis, University of Colorado, 2022.

[13] Hartmann, P., Meyer, C., and Moormann, D., “Unified Velocity Control and Flight State Transition of Unmanned Tilt-Wing Aircraft,” *Journal of Guidance, Control, and Dynamics*, Vol. 40, No. 6, 2017, pp. 1348–1359. https://doi.org/10.2514/1.g002168.

[14] Fredericks, W. J., McSwain, R. G., Beaton, B. F., and Klassman, D. F., “Greased Lightning (GL-10) Flight Testing Campaign,” Tech. Report TM–2017-219643, NASA, Hampton, Virginia, Jul. 2017.

[15] Betts, J. T., *Practical Methods for Optimal Control and Estimation Using Nonlinear Programming - Second Edition*, SIAM, 2010.

[16] Doff-Sotta, M., Cannon, M., and Bacic, M., “Fast Optimal Trajectory Generation for a Tiltwing VTOL Aircraft with Application to Urban Air Mobility,” *2022 American Control Conference (ACC)*, IEEE, 2022, pp. 4036–4041. https://doi.org/10.23919/acc53348.2022.9867852.

[17] Chauhan, S. S., and Martins, J. R. R. A., “Tilt-Wing eVTOL Takeoff Trajectory Optimization,” *Journal of Aircraft*, Vol. 57, No. 1, 2020, pp. 93–112. https://doi.org/10.2514/1.C035476.

[18] Panish, L., and Bacic, M., “Transition Trajectory Optimization for a Tiltwing VTOL Aircraft with Leading-Edge Fluid Injection Active Flow Control,” *AIAA SciTech 2022 Forum*, AIAA, 2022. https://doi.org/10.2514/6.2022-1082.

[19] Doff-Sotta, M., Cannon, M., and Bacic, M., “Data-Driven Robust Model Predictive Control of Tiltwing Vertical Takeoff and Landing Aircraft,” *Journal of Guidance, Control, and Dynamics*, 2024, pp. 1–9. https://doi.org/10.2514/1.g008315.

[20] Yang, Y., Zhu, J., Wang, X., Yuan, X., and Zhang, X., “Dynamic Transition Corridors and Control Strategy of a Rotor-Blown-Wing Tail-Sitter,” *Journal of Guidance, Control, and Dynamics*, Vol. 44, No. 10, 2021, pp. 1836–1852. https://doi.org/10.2514/1.g005464.

[21] Li, B., Sun, J., Zhou, W., Wen, C.-Y., Low, K. H., and Chen, C.-K., “Transition Optimization for a VTOL Tail-Sitter UAV,” *IEEE/ASME Transactions on Mechatronics*, Vol. 25, No. 5, 2020, pp. 2534–2545. https://doi.org/10.1109/tmech.2020.2983255.

[22] Oosedo, A., Abiko, S., Konno, A., and Uchiyama, M., "Optimal Transition from Hovering to Level-Flight of a Quadrotor Tail-Sitter UAV," *Autonomous Robots*, Vol. 41, No. 5, 2016, pp. 1143–1159. https://doi.org/10.1007/s10514-016-9599-4.

[23] Kubo, D., and Suzuki, S., "Tail-Sitter Vertical Takeoff and Landing Unmanned Aerial Vehicle: Transitional Flight Analysis," *Journal of Aircraft*, Vol. 45, No. 1, 2008, pp. 292–297. https://doi.org/10.2514/1.30122.

[24] McIntosh, K., Reddinger, J., Mishra, S., and Zhao, D., "Optimal Trajectory Generation for Transitioning Quadrotor Biplane Tailsitter Using Differential Flatness," *Proceedings of the Vertical Flight Society 77th Annual Forum*, The Vertical Flight Society, 2021, pp. 1–9. https://doi.org/10.4050/f-0077-2021-16858.

[25] Tal, E., Ryou, G., and Karaman, S., "Aerobatic Trajectory Generation for a VTOL Fixed-Wing Aircraft Using Differential Flatness," *IEEE Transactions on Robotics*, Vol. 39, No. 6, 2023, pp. 4805–4819. https://doi.org/10.1109/tro.2023.3301312.

[26] Rieck, R. M., "Discrete Controls and Constraints in Optimal Control Problems," Ph.D. thesis, Technische Universität München, 2017.

[27] Nie, Y., Faqir, O., and Kerrigan, E. C., "ICLOCS2: Try this Optimal Control Problem Solver Before you Try the Rest," *2018 UKACC 12th International Conference on Control (CONTROL)*, IEEE, 2018. https://doi.org/10.1109/control.2018.8516795.

[28] Wächter, A., and Biegler, L. T., "On the Implementation of an Interior-Point Filter Line-Search Algorithm For Large-Scale Nonlinear Programming," *Mathematical Programming*, Vol. 106, No. 1, 2005, pp. 25–57. https://doi.org/10.1007/s10107-004-0559-y.

[29] May, M. S., Milz, D., and Looye, G., "Dynamic Modeling and Analysis of Tilt-Wing Electric Vertical Take-Off and Landing Vehicles," *AIAA SciTech 2022 Forum*, AIAA, 2022. https://doi.org/10.2514/6.2022-0263.

[30] Leishman, J. G., *Principles of Helicopter Aerodynamics*, Cambridge University Press, 2000, p. 62.

[31] McCormick, B. W., *Aerodynamics of V/STOL Flight*, Dover Publications, Mineola, N.Y, 1999, pp. 96–99.

[32] Montgomerie, B., *Methods for Root Effects, Tip Effects and Extending the Angle of Attack Range to +- 180°, with Application to Aerodynamics for Blades on Wind Turbines and Propellers*, Swedish Defence Research Agency, Stockholm, 2004.

[33] Olson, E. D., "Semi-Empirical Prediction of Aircraft Low-Speed Aerodynamic Characteristics," *53rd AIAA Aerospace Sciences Meeting*, AIAA, 2015. https://doi.org/10.2514/6.2015-1679.

[34] Kirkpatrick, D. G., and Murphy, R. D., "Planning Wind-Tunnel Test Programs for V/STOL Conversion Studies," *AIAA 3rd Aerodynamic Testing Conference*, 1968.

[35] Milz, D., May, M. S., and Looye, G., "Dynamic Inversion-Based Control Concept for Transformational Tilt-Wing eVTOLs," *AIAA SciTech 2024 Forum*, AIAA, 2024. https://doi.org/10.2514/6.2024-1290.